





Cite this: DOI: 10.1039/c7nr09684d

Received 28th December 2017,
Accepted 10th March 2018

DOI: 10.1039/c7nr09684d

rsc.li/nanoscale

Touching the theoretical capacity: synthesizing cubic $\text{LiTi}_2(\text{PO}_4)_3/\text{C}$ nanocomposites for high-performance lithium-ion battery†

Wenjun Deng,^a Xusheng Wang,^b Chunyi Liu,^a Chang Li,^a Mianqi Xue,^a  *^{a,b} Rui Li^{*a} and Feng Pan ^a

A cubic $\text{LiTi}_2(\text{PO}_4)_3/\text{C}$ composite is successfully prepared via a simple solvothermal method and further glucose-pyrolysis treatment. The as-fabricated LTP/C material delivers an ultra-high reversible capacity of 144 mA h g^{-1} at 0.2C rate, which is the highest ever reported, and shows considerable performance improvement compared with before. Combining this with the stable cycling performance and high rate capability, such material has a promising future in practical application.

Rechargeable lithium-ion batteries (LIBs) and related series products have enriched many aspects of our daily lives. Now the energy density and power density in electrode materials have reached a plateau.^{1–5} The realization of full capacity delivery is a promising way to solve this problem, with the highly modified LiFePO_4 cathode as example.^{6,7} As a well-known sodium super-ionic conductor (NASICON)-type compound,⁸ $\text{LiTi}_2(\text{PO}_4)_3$ (LTP), which has attracted considerable interest due to its high ion conductivity in the fields of solid-state electrolytes and rechargeable lithium-/sodium-ion batteries,^{9–12} has not achieved its theoretical capacity of 138 mA h g^{-1} in previous work.

The core concept in realizing the theoretical capacity is improvement of the electronic conductivity and the ion-transport rate of the electrode materials, which can begin with two aspects, one being nanocrystallization *via* different micro/nano fabrication methods and the other being composite formation (both aim at reducing the path length of inward ion diffusion and enhancing the resistance to structural pulverization).^{13–22} When it comes to LTP, composition change of material by doping to enhance the transport properties,^{23–25} size reduction of the active material to shorten the ion-transport pathway,^{26,27}

and introduction of a conductive network to improve the electron-transport rate^{28,29} have been developed to attempt to fulfil the goal of full capacity delivery.

In this work, we successfully fabricate a carbon-coated cubic LTP nanocomposite for the first time *via* a facile solvothermal method and further glucose-pyrolysis treatment. The cubic LTP/C nanocomposite delivers an unprecedented capacity of 144 mA h g^{-1} , which is the highest ever reported and exceeds the theoretical capacity. The nanostructure and C–O bond contribute to the extra capacity. Furthermore, the material exhibits considerable capacity retention of 96.1% at 1C after 100 cycles. Moreover, an aqueous rechargeable lithium battery (ARLB) system with LiMn_2O_4 (LMO) as the cathode and cubic LTP/C nanocomposite as the anode presents excellent cycling stability and high rate capability, which could meet the requirements for large-scale energy-storage devices and high-power applications.

Fig. 1a exhibits the X-ray diffraction (XRD) patterns of the as-prepared LTP nanocubes and cubic LTP/C nanocomposite. The results indicate that the prepared sample is pure phase (without any impurity phases such as TiO_2 and TiP_2O_7). All the peaks of the LTP nanocubes and LTP/C nanocomposite can be indexed based on JCPDS no. 35-0754. There are no features of crystalline carbon in any of the four samples, suggesting that the carbon coating is amorphous in nature, and does not affect the crystal structure of LTP.^{8,30} In addition, cubic TiP_2O_7 impurity is observed in the XRD patterns of LTP1/C and LTP2/C (Fig. 1b), especially in LTP1/C. The sharp characteristic peaks appearing at 22.53° , 25.25° and 27.68° can be indexed to cubic phase TiP_2O_7 (JCPDS: 38-1468). These peaks become very low in LTP2/C (the solvothermal temperature raised to 250°C), demonstrating the rapid decrease of the impurities. The impurity phases disappear completely in LTP/C through prolonging the reaction time from 24 to 48 h. It should be specially mentioned that the reaction temperature in fabricating LTP is far lower than that in the traditional solid-state reaction synthesis (even more than 1000°C).³¹

The morphologies of the LTP1/C, LTP2/C and LTP/C nanocomposites were assessed by scanning electron microscopy

^aSchool of Advanced Materials, Peking University Shenzhen Graduate School, Shenzhen 518055, PR China. E-mail: lirui@pkusz.edu.cn, xuemq@iphy.ac.cn

^bInstitute of Physics and Beijing National Laboratory for Condensed Matter Physics, Chinese Academy of Sciences, Beijing 100190, PR China

† Electronic supplementary information (ESI) available: Experimental section, morphology characterization, other electrochemical performances. See DOI: 10.1039/c7nr09684d

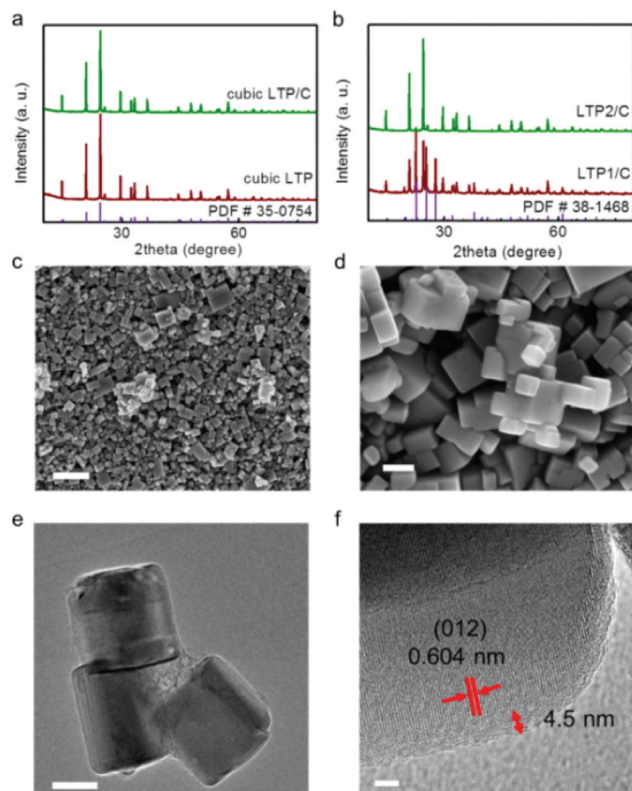


Fig. 1 (a) XRD patterns of LTP nanocube and cubic LTP/C nanocomposites. (b) XRD patterns of LTP1/C and LTP2/C nanocomposites. (c, d) SEM images of the cubic LTP/C nanocomposites at different magnifications. (e) TEM image of the cubic LTP/C nanocomposite. (f) High-resolution TEM (HRTEM) image of the LTP/C nanocomposite. Scale bars are 1 μm , 200 nm, 100 nm, and 5 nm in panels (c–f), respectively.

(SEM) (Fig. 1c, d and Fig. S1†). The results show that the morphology of the LTP is mainly controlled by reaction temperature. For LTP1/C, with the reaction conditions of 160 $^{\circ}\text{C}$ for 24 h, LTP presents short, rod-like appearance with length around 100–200 nm, as shown in Fig. S1a and b.† With the solvothermal temperature raised to 250 $^{\circ}\text{C}$, the morphology of the LTP2/C changes to a not completely regular cubic appearance while remaining in the nanoscale. LTP/C with cubic morphology and smooth surfaces (as shown in Fig. 1c and d) was finally fabricated successfully through the further extension of reaction time to 48 h. Fig. 1e and f severally illustrate the transmission electron microscopy (TEM) and high-resolution TEM (HRTEM) images of the LTP/C nanocomposites. Fig. 1e clearly reveals that the particle size is around 200 nm, which is consistent with the morphology in Fig. 1d. The HRTEM shows that the average thickness of the amorphous carbon layer is about 4.5 nm. The total amount of carbon in LTP/C nanocomposites was estimated to be 4.4 wt% through thermogravimetric analysis (performed on a Mettler-Toledo TGA/DSC1). The uniformly coated carbon layers on each LTP cube are favourable to improve the electronic conductivity.³² The lattice-fringe distance deduced from Fig. 1f is 0.604 nm, which agrees well with the (012) crystal plane of rhombohedral LTP.

The surface chemical states of the LTP/C were assessed through X-ray photoelectron spectroscopy (XPS). In Fig. S2a,† the survey spectrum of LTP/C demonstrates the presence of C, O, P, and Ti elements. For the C 1s region of LTP/C shown in Fig. S2b,† the peak-fitting deconvolution reveals one carbon-related peak located at 284.6 eV (C–C bond), and two oxygen-related peaks located at 285.9 (C–O bond) and 288.7 (C=O bond) eV.^{33,34} The elemental composition of the LTP/C was qualitatively and quantitatively determined by energy dispersive X-ray spectroscopy (EDS) as shown in Fig. S3.† The mappings reveal the homogeneous distributions of P, Ti, O, and C elements; the atomic ratio of Ti : P : O : C is 9.7 : 14.3 : 57.5 : 18.5.

The electrochemical performances at a scan rate of 0.1 mV s^{-1} of the three samples (LTP/C, LTP1/C and LTP2/C) were evaluated in a half cell using a lithium plate as counter-electrode (Fig. 2a). Only one pair of redox peaks is observed for the cubic LTP/C sample. The sharp reduction and oxidation peaks are located at 2.38 V and 2.60 V, revealing a two-phase reaction mechanism.³⁵ In contrast, there are two pairs of redox peaks for LTP1/C and LTP2/C samples, with the extra redox peaks located at around 2.55 V and 2.68 V. These two peaks correspond to the lithium insertion and extraction of the TiP_2O_7 phase,³⁶ identical with the XRD results. Fig. 2b and Fig. S4† exhibit the capacity of LTP/C, LTP1/C and LTP2/C as a function

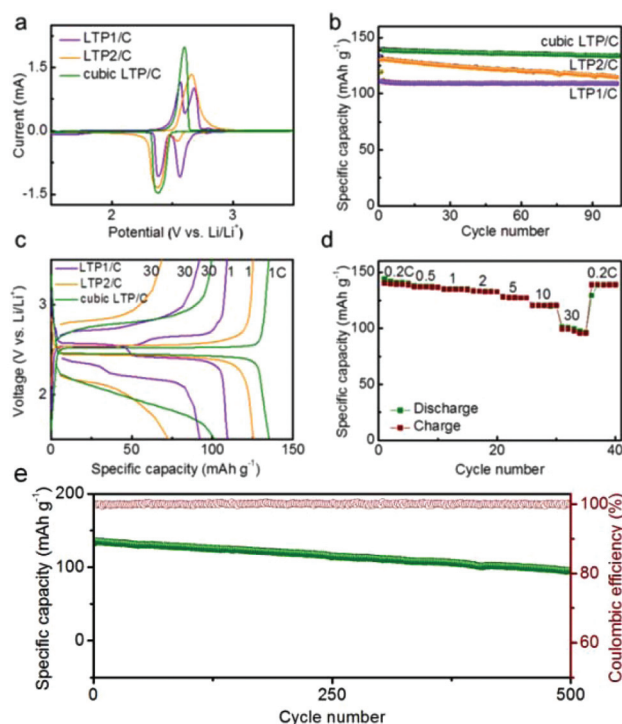


Fig. 2 (a) Typical cyclic voltammetry (CV) curves of LTP1/C, LTP2/C and LTP/C nanocomposites at a scan rate of 0.1 mV s^{-1} . (b) Cycling performance of the three samples at 1C (1C = 140 mA g^{-1}). (c) Galvanostatic voltage profiles of the three samples at 1C and 30C. (d) Rate capability of the cubic LTP/C nanocomposites. (e) The cycling performance of LTP/C at 5C.

of cycle number. The initial discharge capacities are 140, 133, and 120 mA h g⁻¹ for cubic LTP/C, LTP2/C and LTP1/C, respectively. The initial charge–discharge efficiencies are 99.4%, 98.1% and 93.0% for these three samples, which are favourable for practical applications. The capacity retention values compared with the initial capacity are 96.2%, 86.3% and 91.3% after 100 cycles at 1C, with a subsequent coulombic efficiency of ~100%, indicating that the electrochemical reaction of cubic LTP/C is highly reversible and stable.

The galvanostatic voltage profiles of the three LTP-based samples at 1 and 30C are illustrated in Fig. 2c, which shows that the discharge capacity of cubic LTP/C slightly decreases from 139 to 102 mA h g⁻¹ while current rate increases from 1 to 30C. The high reversible capacity at a current rate as much as 30C indicates high rate capability. However, the discharge capacities maintain only 93 and 74 mA h g⁻¹ at 30C for LTP1/C and LTP2/C, respectively. Furthermore, only one well-defined platform is observed for the LTP/C electrode, which is different from LTP1/C and LTP2/C with two platforms. The platform with higher voltage is due to the Ti₂O₇ phase, which agrees well with the cyclic voltammetry (CV) and XRD results. Furthermore, the rate capability of the LTP/C electrodes was evaluated at 0.2, 0.5, 1, 2, 5, 10 and 30C every five cycles (Fig. 2d). The long-term cycling stability of LTP/C was also assessed at 5C (Fig. 2e); after 500 cycles, the LTP/C electrode still delivers a reversible capacity of 95 mA h g⁻¹ with a retention of 71.2%. Parallel battery tests (different batteries and batch samples, respectively, Fig. S5†) at 0.2C indicate the good reproducibility and strength of the capacity delivery of LTP/C. The higher than theoretical capacity could be attributed to the special cubic nanostructure and C–O bond.^{37–39} Similarly to our previous finding that the surface C–O–Fe bonds can induce extra surface lithium storage for LiFePO₄/carbon nanoparticles,³⁸ here we also attributed the extra capacity in LTP/carbon to the larger content of C–O groups in the LTP surface, which comes from the C–O–Ti/Li bonds at the LTP/carbon interface. This hypothesis is reasonable, given that there are unpassivated Ti and Li atoms at the surface of LTP. For the original surface of LTP without C–O–Ti/Li bonds, the dangling Ti, Li, and O are self-passivated for charge compensation to satisfy the electron counting rule. Thus, there is no excess dangling O to bond with extra Li-ions at the LTP surface. By contrast, at the LTP/carbon interface, the dangling Ti and Li bond with the C–O–Ti/Li groups instead of the original dangling O bonds at the surface. These surface dangling O atoms would bond strongly with excess Li at the LTP surface, thus introducing extra Li-ion storage. Meanwhile, the original truncated surface Li-ions are also compensated by the C–O–Ti/Li bonds, which also helps increase the binding energy of the original surface Li-ions. Fig. S6a† shows experimental charge–discharge curves of the bare LTP and LTP/C samples in the initial three cycles at 0.2C. The extra capacity compared with bare LTP is attributed to the larger content of C–O groups in the LTP/carbon interface, which can be observed in Fig. S6b and c.† The surface composition of LTP/C was checked by XPS with Ar⁺ sputtering. The dominant carbon-containing functional

groups at the LTP/carbon surface are C–C, C–O, and carbonyls (C=O). The main peaks centred at 284.6 ± 0.2 eV correspond to graphitic carbon, and the independent peaks at 285.6 ± 0.2 eV and 288.6 ± 0.2 eV can be assigned to the C–O bond and carbon in carbonyl groups (C=O), respectively. The XPS peak areas were used to estimate the amount of each species on the surface (Table S1†); even after etching for 30 s (about 6 nm in depth), the amount of C–O bonds was still 26.8%, indicating the larger content of C–O–Ti/Li bonds at the LTP/carbon interface to introduce extra Li-ion storage. The excellent capacity–recovery capability was revealed when the current rate was changed back to 0.2C. Obviously, the high capacity, remarkable cycling stability and superior rate performance of the cubic LTP/C nanocomposite could be attributed to the advantages of its cubic morphology and pure phase structure. To our best knowledge, the specific capacity of the fabricated cubic LTP/C nanocomposite is the highest ever reported,^{9,11,27,29,31,40–46} and shows a considerable performance improvement compared with before.

A further *ex situ* XRD test was carried out to investigate the electrochemical reaction mechanism of LTP/C. Fig. 3a shows the *ex situ* XRD patterns of the electrode at different discharged states. The positions of XRD peaks shift gradually toward smaller angle (lines 1 and 2), implying a small increase of lattice parameter during the Li⁺ insertion process.⁴⁷ After that, new diffraction peaks at 14.5°, 19.8°, 24.3° and 29.1° appear when the electrode was discharged to half (point 3). These peaks can be indexed with a rhombohedral system with *a* = *b* = 8.397 Å and *c* = 22.880 Å (Li₃Ti₂(PO₄)₃ JCPDS: 40-0095), indicating a phase transformation during this procedure. In the following discharge process (points 4 and 5), the peak positions of the XRD patterns keep unchanged, except for

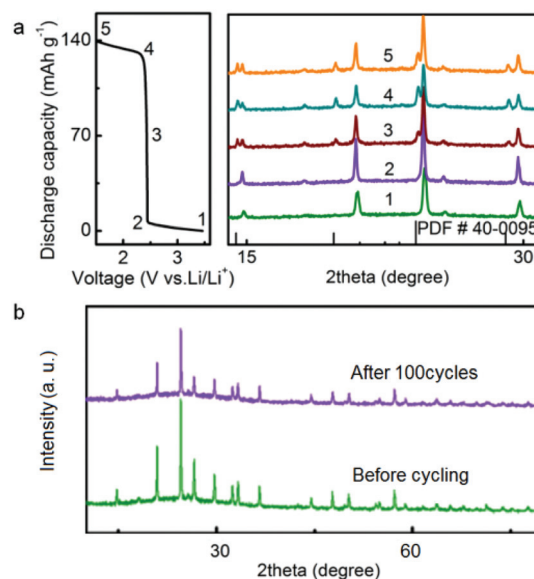
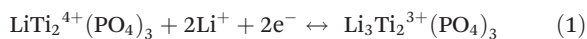


Fig. 3 (a) *Ex situ* XRD patterns of cubic LTP/C electrode at various discharged states. (b) Corresponding XRD patterns before and after 100 cycles.

slightly changed diffraction intensities. Hence, based on these *ex situ* XRD results, the redox mechanism can be considered to be the following equilibrium:



The structure and surface morphology evolution of the cubic LTP/C electrodes were investigated in depth. Fig. S7† and Fig. 3b show the morphology and XRD patterns of the LTP/C electrodes before cycling and after 100 cycles at 1C. Through comparison of Fig. S7a and S7b,† it can be found that the LTP/C electrode maintains its architecture very well after 100 cycles. Further comparison of the nanocubes before and after cycling reveals that their surface becomes rough from fairly smooth, which may be attributed to the formation of a solid electrolyte interface (SEI) film, indicating that the LTP/C nanocubes can accommodate large mechanical strain and volume variation during Li^+ insertion and extraction. Meanwhile, the XRD pattern of the LTP/C electrode after 100 cycles is consistent with the original (Fig. 3b). The only change of the peak strength should be due to the change in surface roughness of the electrode.⁴⁸ Therefore, both the SEM and XRD results imply excellent structural stability of LTP/C nanocubes.

The ARLB based on LMO//LTP/C was constructed using 1 M lithium bis(trifluoromethanesulfonyl)imide (LiTFSI) aqueous solution as the electrolyte (the morphology of the LMO is shown in Fig. S8,† and the XRD pattern of the LMO is shown in Fig. S9a†). The mass ratio of cathode and anode materials was designed to be $\sim 1.5:1$. The electrochemical properties of such batteries were further evaluated between 1.0 and 1.85 V at different current density. First, lithium intercalation and deintercalation behaviours of LMO and LTP/C electrodes in aqueous LiTFSI electrolyte were investigated by CV measurement (as shown in Fig. 4a). There are two pairs of redox peaks for commercial LMO. The reduction peaks are located at 0.88 and 0.99 V (*vs.* saturated calomel electrode (SCE)), and the oxidation peaks are located at 0.95 and 1.07 V (*vs.* SCE), respectively. The results agree well with the intercalation and deintercalation of Li^+ into/from the two different lattice sites in LMO.^{49,50} On the other hand, only one pair of Li^+ insertion/extraction peaks at -0.54 and -0.72 V (*vs.* saturated calomel electrode (SCE)) is observed in the cubic LTP/C, which is consistent with the behaviours of the LTP/C electrode in non-aqueous electrolyte (as shown in Fig. 2a). Fig. 4b shows the charge–discharge curves and cycle performance at 1C. The ARLB shows excellent reversibility with a flat voltage profile centred at 1.5 V, while the first discharge capacity can reach 126 mA h g^{-1} (based on the mass of LTP/C) with a high initial charge–discharge efficiency of 90.1%. Furthermore, the battery delivers a capacity of 106 mA h g^{-1} after 200 cycles with corresponding coulombic efficiency of $\sim 100\%$ (the capacity retention is 84.8%, as shown in Fig. 4b and c). Fig. 4d shows the rate performance of the ARLB. The reversible capacities are 124, 115, 106, 95, and 80 mA h g^{-1} at current rates of 0.5, 1, 2, 5, and 10C, respectively. The rate capability of the ARLB is poorer than that of the LTP/C half cell, because it is greatly limited by

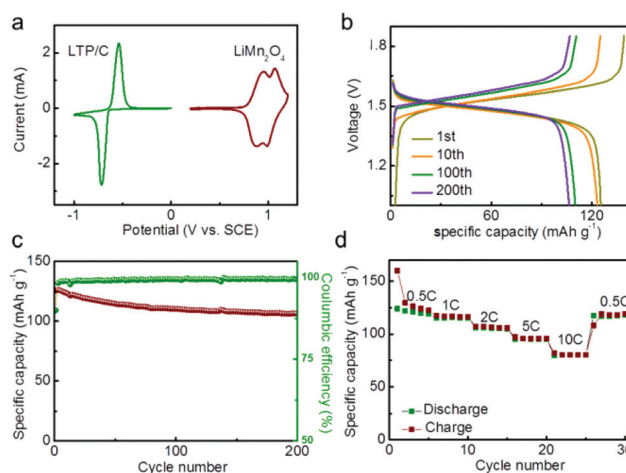


Fig. 4 (a) CV curves of LTP/C and LMO electrodes in 1 M LiTFSI aqueous solution at a scan rate of 0.5 mV s^{-1} , measured by a three-electrode system using a platinum electrode as the counter-electrode and a saturated calomel electrode (SCE) as the reference electrode. (b) Charge–discharge curves of LTP/C//LMO ARLB at 1C. (c) Cycling performance of the ARLB at 1C. (d) Rate capability of the LTP/C//LMO ARLB.

the LMO cathode (Fig. S9b†). However, the rate performance of such an ARLB is still much better than previous reports.^{9,44,51,52} Especially, the ARLB presents excellent capacity and cycling performance even at a high current rate of 10C (Fig. S10†). Furthermore, the ARLB presents a high specific energy density of 63 W h kg^{-1} at a power density of 420 W kg^{-1} based on the total mass of cathode and anode active materials, which competes with lead–acid technology.

In summary, an LTP/C nanocube composite has been synthesized for the first time *via* a simple solvothermal method and further glucose-pyrolysis treatment. The as-fabricated LTP/C nanocube composite delivers an ultra-high reversible capacity of 144 mA h g^{-1} at 0.2C, which is the highest ever reported and shows considerable performance improvement compared with before. This result exceeds the theoretical capacity, which should be attributed to its specific cubic nanostructure and C–O bond. Combining this with the stable cycling performance (capacity retention of 96.1% after 100 cycles) and high rate capability (102 mA h g^{-1} at 30C), the LTP/C nanocube composite has a promising future in practical application. In addition, the further *ex situ* XRD study demonstrates a two-phase reaction mechanism. More importantly, the ARLB system with LMO as the cathode and LTP/C nanocube composite as the anode presents high cycling stability (capacity retention of 84.8% after 200 cycles at 1C) and high rate capability (80 mA h g^{-1} at 10C). Hence, the LTP/C nanocube composite should be paid more attention to target high-performance (aqueous) lithium-ion batteries.

Conflicts of interest

There are no conflicts to declare.

Acknowledgements

This work was supported by the Shenzhen Science and Technology Research Grant (JCYJ20160531141109132, JCYJ20170412150450297), the National Natural Science Foundation of China (21622407) and Guangdong Innovative and Entrepreneurial Research Team Progress (2013N080).

Notes and references

- J. Lu, Z. Chen, Z. Ma, F. Pan, L. A. Curtiss and K. Amine, *Nat. Nanotechnol.*, 2016, **11**, 1031.
- J. W. Choi and D. Aurbach, *Nat. Rev. Mater.*, 2016, **1**, 16013.
- B. Scrosati and J. Garche, *J. Power Sources*, 2010, **195**, 2419–2430.
- Y. Wei, J. Zheng, S. Cui, X. Song, Y. Su, W. Deng, Z. Wu, X. Wang, W. Wang, M. Rao, Y. Lin, C. Wang, K. Amine and F. Pan, *J. Am. Chem. Soc.*, 2015, **137**, 8364–8367.
- X. Rui, Q. Yan, M. Skyllas-Kazacos and T. M. Lim, *J. Power Sources*, 2014, **258**, 19–38.
- S. Lim, C. S. Yoon and J. Cho, *Chem. Mater.*, 2008, **20**, 4560–4564.
- C. Gong, F. Deng, C.-P. Tsui, Z. Xue, Y. S. Ye, C.-Y. Tang, X. Zhou and X. Xie, *J. Mater. Chem. A*, 2014, **2**, 19315–19323; D. Rangappa, M. Ichihara, T. Kudo and I. Honma, *J. Power Sources*, 2009, **194**, 1036–1042.
- L. Zhang, X. Wang, W. Deng, X. Zang, C. Liu, C. Li, J. Chen, M. Xue, R. Li and F. Pan, *Nanoscale*, 2018, **10**, 958–963.
- J.-Y. Luo and Y.-Y. Xia, *Adv. Funct. Mater.*, 2007, **17**, 3877–3884.
- B. Lang, B. Ziebarth and C. Elsaesser, *Chem. Mater.*, 2015, **27**, 5040–5048; Z. Yang, H. Liang, X. Wang, X. Ma, T. Zhang, Y. Yang, L. Xie, D. Chen, Y. Long, J. Chen, Y. Chang, C. Yan, X. Zhang, X. Zhang, B. Ge, Z. Ren, M. Xue and G. Chen, *ACS Nano*, 2016, **10**, 755–762.
- V. Aravindan, W. C. Ling, S. Hartung, N. Bucher and S. Madhavi, *Chem. – Asian J.*, 2014, **9**, 878–882.
- H. Aono, E. Sugimoto, Y. Sadaoka, N. Imanaka and G. Adachi, *J. Electrochem. Soc.*, 1990, **137**, 1023–1027.
- M. Xue, Y. Wang, X. Wang, X. Huang and J. Ji, *Adv. Mater.*, 2015, **27**, 5923–5929; M. Xue, D. Chen, Y. Long, P. Wang, L. Zhao and G. Chen, *Adv. Mater.*, 2015, **27**, 3614–3619.
- A. S. Arico, P. Bruce, B. Scrosati, J. M. Tarascon and W. Van Schalkwijk, *Nat. Mater.*, 2005, **4**, 366–377.
- X. Ma, M. Xue, F. Li, J. Chen, D. Chen, X. Wang, F. Pan and G. Chen, *Nanoscale*, 2015, **7**, 8715–8719.
- M. Xue, F. Li and T. Cao, *Nanoscale*, 2012, **4**, 1939–1947; M. Xue, F. Li, Y. Wang, X. Cai, F. Pan and J. Chen, *Nanoscale*, 2013, **5**, 1803–1805.
- X. Wang, D. Chen, Z. Yang, X. Zhang, C. Wang, J. Chen, X. Zhang and M. Xue, *Adv. Mater.*, 2016, **28**, 8645–8650.
- J. Maier, *Nat. Mater.*, 2005, **4**, 805–815.
- M. Xue, D. Chen, X. Wang, J. Chen and G. F. Chen, *J. Mater. Chem. A*, 2015, **3**, 7715–7718.
- D. W. Wang, F. Li, M. Liu, G. Q. Lu and H. M. Cheng, *Angew. Chem., Int. Ed.*, 2009, **48**, 1525–1525.
- M. Xue, X. Ma, Z. Xie, L. Duan, Y. Jiang, M. Zhang and T. Cao, *Chem. – Asian J.*, 2010, **5**, 2266–2270.
- H. Sun, L. Mei, J. Liang, Z. Zhao, C. Lee, H. Fei, M. Ding, J. Lau, M. Li, C. Wang, X. Xu, G. Hao, B. Papandrea, I. Shakir, B. Dunn, Y. Huang and X. Duan, *Science*, 2017, **356**, 599–604.
- W. Zając, M. Tarach and A. Trenzczek-Zając, *Acta Mater.*, 2017, **140**, 417–423.
- K. Arbi, S. Mandal, J. M. Rojo and J. Sanz, *Chem. Mater.*, 2002, **14**, 1091–1097.
- J. Kuwano, N. Sato, M. Kato and K. Takano, *Solid State Ionics*, 1994, **70**, 332–336.
- Y. Xu, C. Xu, Q. An, Q. Wei, J. Sheng, F. Xiong, C. Pei and L. Mai, *J. Mater. Chem. A*, 2017, **5**, 13950–13956.
- M. Zhou, L. Liu, L. Yi, Z. Yang, S. Mao, Y. Zhou, T. Hu, Y. Yang, B. Shen and X. Wang, *J. Power Sources*, 2013, **234**, 292–301.
- D. Sun, X. Xue, Y. Tang, Y. Jing, B. Huang, Y. Ren, Y. Yao, H. Wang and G. Cao, *ACS Appl. Mater. Interfaces*, 2015, **7**, 28337–28345.
- S. Yu, H. Tempel, R. Schierholz, O. Aslanbas, X. Gao, J. Mertens, L. G. J. de Haart, H. Kungl and R.-A. Eichel, *ChemElectroChem*, 2016, **3**, 1157–1169.
- H. Liang, X. Ma, Z. Yang, P. Wang, X. Zhang, Z. Ren, M. Xue and G. Chen, *Carbon*, 2016, **99**, 585–590.
- J.-Y. Luo, L.-J. Chen, Y.-J. Zhao, P. He and Y.-Y. Xia, *J. Power Sources*, 2009, **194**, 1075–1080; G. X. Wang, D. H. Bradhurst, S. X. Dou and H. K. Liu, *J. Power Sources*, 2003, **124**, 231–236.
- J. Wang and X. Sun, *Energy Environ. Sci.*, 2012, **5**, 5163–5185.
- C. Yan, J. Wang, W. Kang, M. Cui, X. Wang, C. Y. Foo, K. J. Chee and P. S. Lee, *Adv. Mater.*, 2014, **26**, 2022–2027; X. Zang, X. Wang, Z. Yang, X. Wang, R. Li, J. Chen, J. Ji and M. Xue, *Nanoscale*, 2017, **9**, 19346–19352.
- F. Zhao, S. Dai, Y. Wu, Q. Zhang, J. Wang, L. Jiang, Q. Ling, Z. Wei, W. Ma and W. You, *Adv. Mater.*, 2017, **29**, 1604972.
- S. P. And and C. Masquelier, *Chem. Mater.*, 2002, **14**, 5057–5068.
- V. Aravindan, M. V. Reddy, S. Madhavi, S. G. Mhaisalkar, G. V. S. Rao and B. V. R. Chowdari, *J. Power Sources*, 2011, **196**, 8850–8854.
- C. Lu, D. W. Rooney, X. Jiang, W. Sun, Z. Wang, J. Wang and K. Sun, *J. Mater. Chem. A*, 2017, **5**, 24636–24644.
- Y. Duan, B. Zhang, J. Zheng, J. Hu, J. Wen, D. J. Miller, P. Yan, T. Liu, H. Guo and W. Li, *Nano Lett.*, 2017, **17**, 6018–6026.
- M. Lee, J. Hong, J. Lopez, Y. Sun, D. Feng, K. Lim, W. C. Chueh, M. F. Toney, Y. Cui and Z. Bao, *Nat. Energy*, 2017, **2**, 861–868.
- J.-Y. Luo, J.-L. Liu, P. He and Y.-Y. Xia, *Electrochim. Acta*, 2008, **53**, 8128–8133.
- H. Wang, K. Huang, Y. Zeng, S. Yang and L. Chen, *Electrochim. Acta*, 2007, **52**, 3280–3285.

- 42 V. Aravindan, W. Chuiling, M. V. Reddy, G. V. S. Rao, B. V. R. Chowdari and S. Madhavi, *Phys. Chem. Chem. Phys.*, 2012, **14**, 5808–5814.
- 43 L. Liu, M. Zhou, G. Wang, H. Guo, F. Tian and X. Wang, *Electrochim. Acta*, 2012, **70**, 136–141.
- 44 L. Liu, T. Song, H. Han, H. Park, J. Xiang, Z. Liu, Y. Feng and U. Paik, *J. Mater. Chem. A*, 2015, **3**, 10395–10402.
- 45 J. Sun, Y. Sun, L. Gai, H. Jiang and Y. Tian, *Electrochim. Acta*, 2016, **200**, 66–74.
- 46 D. Sun, Y. Tang, K. He, Y. Ren, S. Liu and H. Wang, *Sci. Rep.*, 2015, **5**, 17452; Z. He, Y. Jiang, W. Meng, J. Zhu, Y. Liu, L. Dai and L. Wang, *Electrochim. Acta*, 2016, **222**, 1491–1500.
- 47 D. Chen, X. Wang, J. Chen, Z. Ren, M. Xue and G. Chen, *Adv. Mater.*, 2015, **27**, 4224–4228.
- 48 H. Wang, K. Huang, C. Huang, S. Liu, Y. Ren and X. Huang, *J. Power Sources*, 2011, **196**, 5645–5650.
- 49 F. Cheng, H. Wang, Z. Zhu, Y. Wang, T. Zhang, Z. Tao and J. Chen, *Energy Environ. Sci.*, 2011, **4**, 3668–3675.
- 50 C. H. Jiang, S. X. Dou, H. K. Liu, M. Ichihara and H. S. Zhou, *J. Power Sources*, 2007, **172**, 410–415.
- 51 J.-Y. Luo, W.-J. Cui, P. He and Y.-Y. Xia, *Nat. Chem.*, 2010, **2**, 760–765.
- 52 D. Sun, Y. Jiang, H. Wang, Y. Yao, G. Xu, K. He, S. Liu, Y. Tang, Y. Liu and X. Huang, *Sci. Rep.*, 2015, **5**, 10733.